
IBO: INPAINTING-BASED OCCLUSION TO ENHANCE EXPLAINABLE ARTIFICIAL INTELLIGENCE EVALUATION IN HISTOPATHOLOGY

A PREPRINT

Pardis Afshar¹, Sajjad Hashembeiki², Pouya Khani³,
Emad Fatemizadeh², and Mohammad Hossein Rohban¹

¹Department of Computer Engineering, Sharif University of Technology, Tehran, Iran

²Department of Electrical Engineering, Sharif University of Technology, Tehran, Iran

³Department of Computer Science, Aarhus University, Aarhus, Denmark
{pafshar, s.hashem, fatemizadeh, rohban}@sharif.edu
pouya.khani@cs.au.dk

ABSTRACT

Histopathological image analysis is crucial for accurate cancer diagnosis and treatment planning. While deep learning models, especially convolutional neural networks, have advanced this field, their "black-box" nature raises concerns about interpretability and trustworthiness. Explainable Artificial Intelligence (XAI) techniques aim to address these concerns, but evaluating their effectiveness remains challenging. A significant issue with current occlusion-based XAI methods is that they often generate Out-of-Distribution (OoD) samples, leading to inaccurate evaluations. In this paper, we introduce Inpainting-Based Occlusion (IBO), a novel occlusion strategy that utilizes a Denoising Diffusion Probabilistic Model to inpaint occluded regions in histopathological images. By replacing cancerous areas with realistic, non-cancerous tissue, IBO minimizes OoD artifacts and preserves data integrity. We evaluate our method on the CAMELYON16 dataset through two phases: first, by assessing perceptual similarity using the Learned Perceptual Image Patch Similarity (LPIPS) metric, and second, by quantifying the impact on model predictions through Area Under the Curve (AUC) analysis. Our results demonstrate that IBO significantly improves perceptual fidelity, achieving nearly twice the improvement in LPIPS scores compared to the best existing occlusion strategy. Additionally, IBO increased the precision of XAI performance prediction from 42% to 71% compared to traditional methods. These results demonstrate IBO's potential to provide more reliable evaluations of XAI techniques, benefiting histopathology and other applications. The source code for this study is available on GitHub¹.

Keywords Histopathology · Histopathological Image Analysis · Cancer Diagnosis · Deep Diffusion Models · Explainable Artificial Intelligence

¹<https://github.com/a-fsh-r/IBO>

1 Introduction

Histopathological image analysis plays a critical role in diagnosing and planning the treatment of cancers, such as breast cancer [1]. Deep learning has significantly advanced the field of breast cancer histopathological image classification [2]. Traditional methods, which relied on extensive manual feature engineering and domain expertise, have been outperformed by modern techniques [3]. Convolutional Neural Network (CNN) architectures, in particular, automate the process of feature extraction and classification directly from raw image data. This automation simplifies the workflow and enhances accuracy, providing a powerful tool in the diagnosis of breast cancer [4].

Despite deep models' high performance, the *black-box* nature of these models raises concerns about their interpretability and transparency [5]. Pathologists and experts need models that not only perform exceptionally well but also clearly explain their decision-making processes [6]. To address this, Explainable Artificial Intelligence (XAI) techniques are being increasingly integrated for explaining machine learning models in various fields, such as computer networking [7], indoor image classification [8], brain-computer interfaces [9], and especially for our case, into histopathological cancer diagnosis [10]. XAI makes the decision-making processes of complex models, such as CNNs, understandable to humans. This transparency is crucial in the medical field, where understanding how Artificial Intelligence (AI) reaches its conclusions can help in clinical validation and build trust among healthcare professionals [11].

However, evaluating the reliability of different XAI methods remains challenging [12]. This challenge highlights the urgent need for effective evaluation frameworks. Given that experts have limited time for manual assessments, automating the evaluation process is essential for ensuring efficient and timely evaluations [13]. Evaluation metrics for XAI methods are typically divided into two categories: qualitative and quantitative. Qualitative metrics, which rely on subjective assessments, contrast sharply with quantitative metrics that offer objective, numerical evaluations. The latter are particularly valuable for their reproducibility, scalability, and their ability to facilitate systematic tuning of models. One major challenge in XAI evaluation is the absence of ground-truth explanations, making it difficult to objectively assess the accuracy and reliability of the explanations generated by different methods. Without a definitive standard, comparing and validating the effectiveness of XAI techniques becomes inherently subjective and complex. In cases where ground-truth is not available, alternative quantitative evaluation methods can be utilized.

Quantitative metrics assess various critical aspects of XAI, such as trustworthiness (often measured as fidelity to the original model's decisions) [14], sensitivity [15] to changes in input, and robustness against variations in data, etc. Among these, fidelity is considered one of the most crucial, as it directly measures how faithfully an explanation represents the decision-making process of the underlying model. To evaluate fidelity, researchers have developed several classes of quantitative metrics, including perturbation-based and occlusion-based metrics [16]. Occlusion-based metrics are among the most well-known ones due to their straightforward implementation and insightful evaluations. These metrics systematically mask input data to observe how changes affect model outputs, thereby providing a clear window into the model's operational dependencies. Using these metrics, the fidelity of XAI methods can be evaluated by assessing how rapidly the model's performance degrades when portions of the input are masked [17].

Existing occlusion strategies in XAI evaluation metrics, such as the Deletion method [18], face significant challenges that undermine their effectiveness. A primary issue arises when these methods attempt to mask or occlude input features, resulting in the transformation of the input sample into an Out-of-Distribution (OoD) or anomalous sample [19]. This transformation introduces ambiguity in the model's behavior change, as it becomes unclear whether the observed change is due to the occlusion itself, the OoD nature, or the anomaly of the modified sample [20]. Consequently, the accuracy and reliability of these occlusion-based metrics are compromised. To address this, there is a critical need for more sophisticated occlusion strategies that minimize the OoD ratio and the introduction of anomalies in occluded samples. Such strategies should ensure that the modified inputs remain within the distribution of the training data, thereby providing a more precise and faithful assessment

of the model’s reliance on specific input features. By reducing the incidence of OoD and anomalous samples, we can achieve a more accurate understanding of the model’s decision-making process and improve the overall robustness of XAI evaluation metrics.

In this paper, we propose a novel occlusion strategy that leverages a diffusion model trained on non-cancerous samples of histopathological images. Our approach involves inpainting cancerous regions with non-cancerous regions as part of a region occlusion process to remove information during the evaluation of XAI methods. By providing more realistic inpainting of occluded regions, our method aims to overcome the limitations of existing techniques, reducing OoD artifacts and anomalies while preserving the integrity of the original data distribution. This framework enhances the reliability of the explanation evaluation process, offering a more trustworthy and efficient explanation method for histopathological image diagnosis.

The remainder of this paper is structured as follows: Section 2 reviews related work, highlighting previous approaches and their limitations. In Section 3, we detail our proposed methodology, including the occlusion strategy using inpainting approach. Section 4 presents our experiments and results, demonstrating the effectiveness of our proposed method. Section 5 discusses the limitations of our study and suggests directions for future work. Finally, Section 6 concludes the paper, summarizing our key findings and contributions to the field of Explainable histopathology images diagnosis and also XAI methods evaluation.

2 Related works

In this section, we highlight that our study closely aligns with two main areas of existing research. Firstly, it pertains to the evaluation of explanation methods, particularly within the realm of medical imaging and specifically histopathology. Our work contributes to this field by providing a more precise evaluation framework, enabling more accurate and reliable comparisons of existing XAI methods. This, in turn, allows us to select the most effective methods for our specific case within the domain of medical imaging. Secondly, our study is related to occlusion strategies within quantitative occlusion-based evaluation metrics. In the following subsections, we will review each of these areas in detail, discussing the most relevant and closely related previous works.

2.1 Explainable AI evaluation

Several studies have compared XAI evaluation metrics to assess their effectiveness and reliability. Kindermans et al. [21] highlighted the (un)reliability of saliency methods, emphasizing the need for robust evaluation frameworks across domains including medical images. Dasgupta et al. [22] proposed a framework for evaluating the faithfulness of local explanations, further contributing to the comparative assessment of XAI methods. Nauta et al. [23] conducted a systematic review on quantitative evaluation methods, providing a detailed comparison across multiple XAI techniques. These studies collectively underscore the importance of systematic and rigorous evaluation metrics in the broader XAI landscape.

In the context of medical imaging, several studies have specifically addressed the evaluation of XAI methods. Lamprou et al. [24] focused on evaluating deep learning interpretability methods for medical images under the scope of faithfulness, providing insights into their applicability and reliability in clinical settings. Furthermore, studies by Rajaraman et al. [25] and Sayres et al. [26] explored the use of deep learning models and integrated gradients [27] explanations in detecting diseases from medical images, demonstrating practical applications and evaluation of XAI methods.

Specifically, for histopathological images, evaluating the effectiveness of XAI methods remains a critical challenge. Graziani et al. [28] provided a comprehensive evaluation of CNN visual explanations in histopathology, offering a comparative analysis of different XAI techniques. Their findings underscore the necessity for domain-specific evaluation metrics to accurately assess and compare interpretability methods in histopathological image analysis.

By integrating these studies, our work contributes to the field by proposing a more precise evaluation framework tailored to medical imaging, particularly histopathology. This enables

more accurate comparisons of existing XAI methods, facilitating the selection of the most effective techniques for specific clinical applications.

2.2 Occlusion strategy

In the evaluation of XAI methods, various strategies have been proposed to occlude features and assess their importance. Blackening [29] involves occluding features by replacing them with black pixels (zero intensity). This straightforward method helps in identifying the importance of specific regions in an image. Given an image I and a binary mask M indicating the regions to be occluded, the blackened image I' is defined as:

$$I' = I \odot (1 - M) \quad (1)$$

where \odot denotes element-wise multiplication. While blackening is easy to implement, it often introduces OoD artifacts, leading to unrealistic samples that do not accurately represent the original data distribution. Another strategy is Blurring [30] that replaces the occluded regions with a Gaussian blur, which maintains the overall structure of the image while removing fine details. Let G be a Gaussian filter, the blurred image I' is given by:

$$I' = I \odot (1 - M) + (I * G) \odot M \quad (2)$$

where \odot denotes element-wise multiplication and $*$ denotes convolution. Blurring reduces OoD artifacts compared to blackening by keeping occluded regions contextually similar to their surroundings. However, when this strategy is applied, the features are not completely deleted or removed due to the blurring effect, which only obscures but does not eliminate the information. In this study [29], they replace occluded regions with the mean pixel value of the dataset, offering a neutral replacement. Let μ be the mean pixel value, then the occluded image I' is:

$$I' = I \odot (1 - M) + \mu \odot M \quad (3)$$

where \odot denotes element-wise multiplication. This method balances maintaining data integrity and avoiding extreme OoD artifacts, providing a middle ground between blackening and blurring. In the Histogram strategy [31], they replace occluded regions with values sampled from the histogram of pixel intensities of the image, maintaining the statistical properties of the original image. For each occluded pixel in P , sample a value from the histogram H of I :

$$I' = I \odot (1 - M) + H \odot M \quad (4)$$

where \odot denotes element-wise multiplication. Histogram-based occlusion preserves local image statistics better than mean replacement and provides a more realistic replacement than blackening or blurring, though it can still introduce some artifacts. Finally, Noisy Linear Imputation (NLI) [32] occludes features by replacing them with values derived from a linear combination of the surrounding observed features, introducing noise to simulate realistic scenarios. This method preserves the local dependencies and adds variability to prevent the model from relying on occlusion artifacts. Given a feature vector \mathbf{x} with a mask \mathbf{m} indicating the occluded regions, the imputed feature vector \mathbf{x}' is computed as:

$$\mathbf{x}' = (1 - \mathbf{m}) \odot \mathbf{x} + \mathbf{m} \odot (\mathbf{X}\hat{\beta} + \epsilon) \quad (5)$$

where \odot denotes element-wise multiplication. Here, \mathbf{X} is the matrix of observed features, $\hat{\beta}$ is the vector of coefficients estimated from a linear model fit to the observed data, and ϵ is a noise term sampled from a normal distribution $\mathcal{N}(0, \sigma^2)$. This approach helps in maintaining the integrity of the model evaluation by ensuring that the imputed features are both realistic and varied, thus providing a more robust assessment of feature importance in XAI tasks. However, the occluded regions remain noticeably different from the rest of the image due to the blurriness.

3 Methodology

The methodology is outlined in the following steps, as illustrated in Figure 1. Our Inpainting-Based Occlusion (IBO) proposed framework involves generating heatmaps to identify

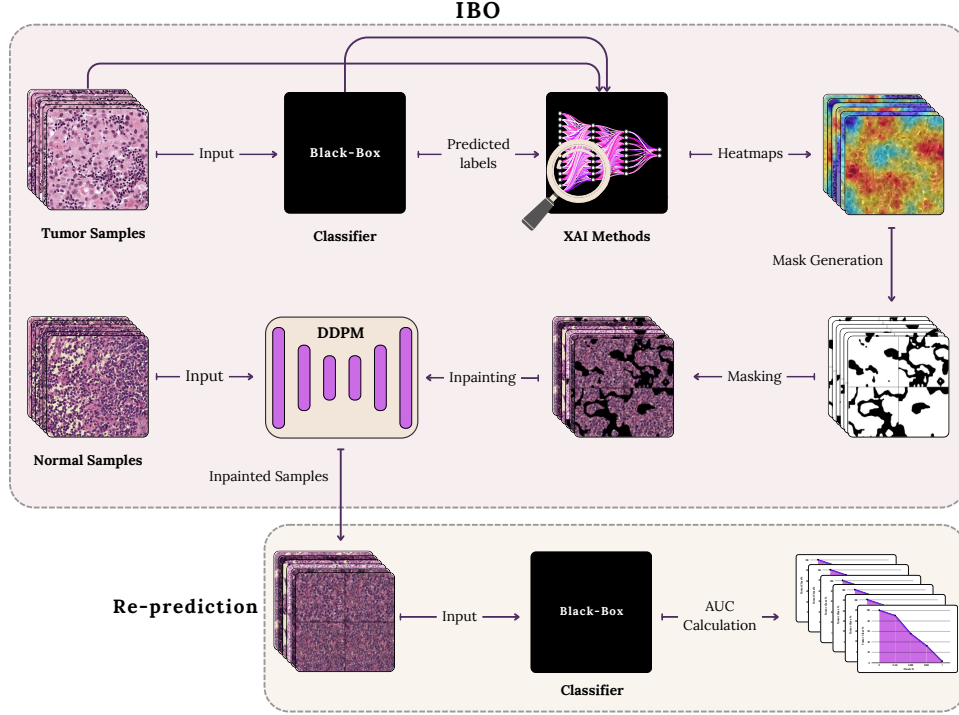


Figure 1: Overview of the methodology used for evaluating XAI methods for breast cancer diagnosis from histopathological images. In Masks, black regions indicate the areas that should be inpainted. These black regions correspond to the tumoric areas identified by the XAI approaches, which are crucial for evaluating the effectiveness of our methodology.

tumoric regions, creating corresponding masks, and then masking the patches based on these masks. We also trained a Denoising Diffusion Probabilistic Model (DDPM) [33] on normal samples to learn the distribution and features of normal tissues. This trained DDPM is then used to inpaint the masked regions, effectively replacing tumoric areas with features typical of normal tissues. Subsequently, we re-predict the inpainted samples using our classifier to predict tumor probabilities. The final step is to calculate the Area Under the Curve (AUC) to assess the impact of the inpainted regions.

3.1 Inpainting

In our study, we utilized RePaint [34], an approach that leverages an unconditional DDPM trained exclusively on normal tissue patches to learn the distribution of normal features. This technique allows us to inpaint regions identified as tumorous in histopathological images, effectively replacing these areas with realistic, normal tissue content. RePaint capitalizes on the DDPM’s capability to generate high-resolution images while maintaining semantic consistency and processing efficiency.

A significant advantage of RePaint is its versatility; it can handle various mask distributions without requiring additional training on specific masks. This adaptability is particularly effective for evaluating and interpreting the significance of features highlighted by different Class Activation Mapping (CAM) [35] techniques, as each XAI approach may produce heatmaps and masks with differing distributions. This variability in mask distributions means the method remains robust across different XAI approaches, ensuring a comprehensive evaluation of feature importance. By inpainting tumorous areas, we can assess the impact of removing these features on the model’s predictions, ensuring the inpainted regions blend seamlessly with their surroundings. However, while RePaint can generate textures that match neighboring areas, the inpainted regions may sometimes lack semantic harmony with the rest of the image. To address this, a novel resampling approach was implemented to improve

the semantic consistency of these regions [34]. This approach involves applying forward transitions to diffuse the output from x_{t-1} back to x_t , scaling back the image and adding noise to preserve information from the generated regions. The generated regions x_t^{unknown} are then updated to be more consistent with the known regions x_t^{known} .

The resampling operation works incrementally, harmonizing one step at a time, which might not fully integrate semantic information across the entire denoising process. To manage this, a jump length j is defined [34], determining the number of forward transitions before applying reverse transitions. In this study, both the jump length and the number of resamplings are set to 10, striking a balance between image quality and computational efficiency, ensuring enhanced semantic consistency and manageable processing time. In Algorithm 1, the procedure of RePaint method is shown.

Algorithm 1 RePaint Algorithm

Require: Image x , Binary mask m where 0 indicates region to be inpainted, Total diffusion steps T , Number of resampling steps U

Ensure: Inpainted image x_0

```

1:  $x_T \sim \mathcal{N}(0, I)$ 
2: for  $t = T$  to 1 do
3:   for  $u = 1$  to  $U$  do
4:      $\epsilon \sim \mathcal{N}(0, I)$  if  $t > 1$ , else  $\epsilon = 0$ 
5:      $x_{t-1}^{\text{known}} = \sqrt{\bar{\alpha}_t}x_0 + (1 - \bar{\alpha}_t)\epsilon$ 
6:      $z \sim \mathcal{N}(0, I)$  if  $t > 1$ , else  $z = 0$ 
7:      $x_{t-1}^{\text{unknown}} = \frac{1}{\sqrt{\bar{\alpha}_t}} \left( x_t - \frac{\beta_t}{\sqrt{1-\bar{\alpha}_t}} \epsilon_\theta(x_t, t) \right) + \sigma_t z$ 
8:      $x_{t-1} = m \odot x_{t-1}^{\text{known}} + (1 - m) \odot x_{t-1}^{\text{unknown}}$ 
9:     if  $u < U$  and  $t > 1$  then
10:       $x_t \sim \mathcal{N}(\sqrt{1 - \beta_{t-1}}x_{t-1}, \beta_{t-1}I)$ 
11:     end if
12:   end for
13: end for
14: return  $x_0$ 

```

Where T denotes the total number of diffusion steps, U is the number of resampling steps at each time step, m represents the mask matrix, and \odot signifies element-wise multiplication. Note that a jump length of $j = 1$ is used in the algorithm above.

3.2 Masking

To support the inpainting process, a clustering approach is employed to segment heatmaps into regions of interest. This segmentation aids in guiding the inpainting procedure by highlighting areas identified as significant by CAM methods. K-means clustering [36] is applied to the grayscale pixel values of each heatmap, which are based on pixel intensity, to partition these pixels into k clusters, with $k = 5$ in this study. The objective of clustering is to minimize the Within-Cluster Sum of Squares (WCSS), which is defined as:

$$\text{WCSS} = \sum_{i=1}^k \sum_{x_j \in C_i} \|x_j - \mu_i\|^2 \quad (6)$$

Here, μ_i represents the centroid of cluster C_i , and x_j is a pixel in that cluster. The algorithm iterates to optimize the centroids and pixel assignments, effectively clustering the grayscale values based on intensity into distinct groups.

In this study, the inpainting process is conducted iteratively, focusing on different regions of the image based on their importance, as indicated by the color intensity of the heatmap. With $k = 5$, the heatmap is divided into five distinct masks, each corresponding to regions of varying significance: I. Red Areas: Most critical regions for model decision-making, II. Red to Yellow Areas: High significance regions, III. Yellow to Green Areas: Moderately important regions, IV. Green to Light Blue Areas: Regions with lower importance, V. Light Blue

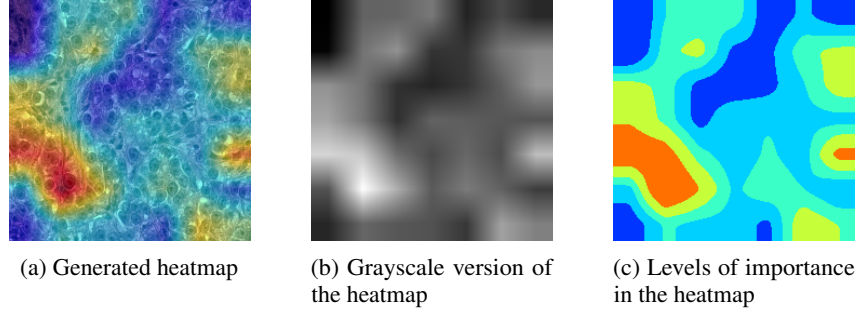


Figure 2: Comparison of generated heatmap, grayscale version of the heatmap, and levels of importance.

to Blue Areas: Least significant regions, often considered non-essential for decision-making and excluded from the inpainting process.

Figures 2a, 2b, and 2c illustrate the generated heatmap, its grayscale version, and the corresponding significance levels. During each inpainting step, only one specific mask (for example, red to yellow areas) is targeted for inpainting. This means that regions corresponding to previously inpainted masks remain unchanged in subsequent steps. The process is cumulative, where the output image from each step is carried forward and further inpainted based on the next mask. As a result, the final inpainted image reflects progressive modifications, with the more critical areas being addressed first, while less significant regions remain unmodified.

3.3 Re-prediction

After the inpainting process, the modified images are reintroduced into the trained classifier for re-prediction, focusing on the classification of each patch. This re-prediction is crucial in determining whether the probability of tumor classification shifts following the removal of the highlighted features. By comparing the classifier’s predictions before and after inpainting, we can critically assess the impact of the identified features on the model’s decision-making process. Furthermore, this approach enables us to evaluate the effectiveness of different XAI methods. The accuracy of each XAI method in pinpointing tumoric regions is measured by observing changes in the model’s predictions, thereby identifying the most reliable and informative heatmaps for feature interpretation.

4 Experiments

In this section, we provide a comprehensive evaluation of our proposed methodology.

4.1 Configuration

CAMELYON16 dataset [37] is a widely recognized benchmark in the field of cancer classification. In our study, we leverage this dataset, which comprises 400 whole slide image (WSI) of sentinel lymph nodes, including 270 slides with precise pixel-level annotations. We further divide these annotated slides into training, validation, and test sets to facilitate our analysis. The dataset provides ground truth data in two formats: Extensible Markup Language (XML) files with contour annotations and WSI binary masks. To evaluate XAI methods, we use the WSI binary masks to calculate the Intersection over Union (IoU) by comparing the masks with the heatmaps generated by these methods. The visual representation of one WSI from the CAMELYON16 dataset is displayed in Figure 3.

As part of the data pre-processing phase, we extract 512×512 pixel patches from each WSI and its corresponding binary mask. This approach ensures that each patch is manageable in size while retaining sufficient detail for analysis. To maintain consistency across histopathological images, we employ stain normalization using the Modified Reinhard method [38].

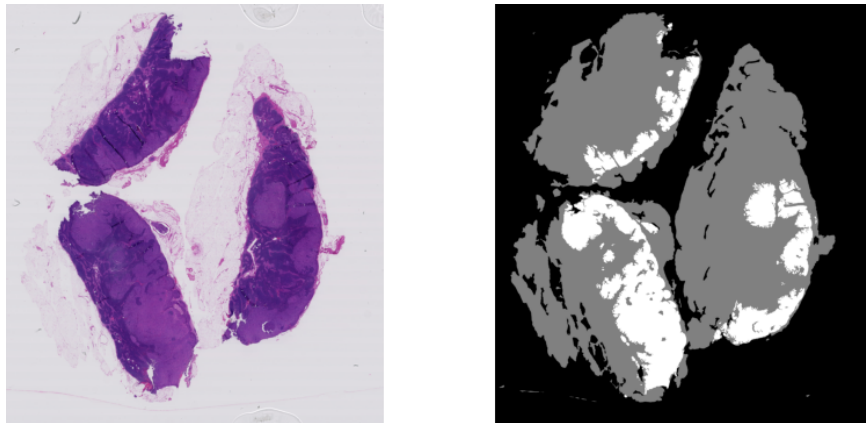


Figure 3: Side-by-side comparison of the WSI (left) and the mask image (right). In the mask image, the white regions indicate tumoric areas.

This technique corrects for variations in staining between different tissue samples and slide preparations by aligning the color distribution of the input images to a reference stain color distribution. By applying stain normalization, we reduce the impact of staining variability on model performance, leading to more accurate and reliable analysis of histopathological images. This step is crucial for improving the consistency and effectiveness of classification and XAI methods.

We trained a ResNet50 [39] model on a dataset of tumor and normal samples extracted from the CAMELYON16 dataset, achieving an impressive overall accuracy of 98.62%. The model demonstrated strong performance with an F1-score of 98.6% in identifying tumor samples, showcasing its high efficacy in distinguishing between tumor and normal tissue. The classifier was trained for 20 epochs using $2 \times T4$ GPUs on the Kaggle platform.

In addition to training the ResNet50 model, we also developed an unconditional DDPM using normal tissue samples from the CAMELYON16 dataset. This training aimed to generate realistic normal tissue samples for data inpainting. The DDPM was trained for 140 epochs on an NVIDIA A100 GPU, ensuring the computational efficiency needed for large-scale histopathological data.

We chose the DDPM for its ability to model complex data distributions and produce high-fidelity samples. By training exclusively on normal samples, the DDPM learned the underlying distribution of non-tumorous tissues, which is useful for inpainting tasks. This approach is especially valuable when dealing with missing or corrupted image regions, as the DDPM can generate plausible tissue structures to fill in the masked areas.

To evaluate the performance of various explanation methods, we applied several CAM-based XAI techniques, including Grad-CAM [40], Grad-CAM++ [41], XGrad-CAM [42], Ablation-CAM [43], Eigen-CAM [44], Score-CAM [45], and Full-Grad [46]. For each tumoric sample, these techniques generated seven different heatmaps. Figure 4 displays the heatmaps generated for a tumoric breast histopathological sample. These heatmaps were then used to create masks, which were applied to various occlusion methods, including our IBO approach.

For performance evaluation, we randomly selected 100 samples from the Tumoric test set. Heatmaps and masks were generated for each sample, and various occlusion strategies, including our proposed method, were applied to evaluate their effectiveness. To handle the computational demands of the IBO approach, we utilized NVIDIA A100 GPUs. Figure 5 displays the original patch, the generated heatmap, and the corresponding masks. Figure 6 illustrates the different occlusion strategies applied to the patch.

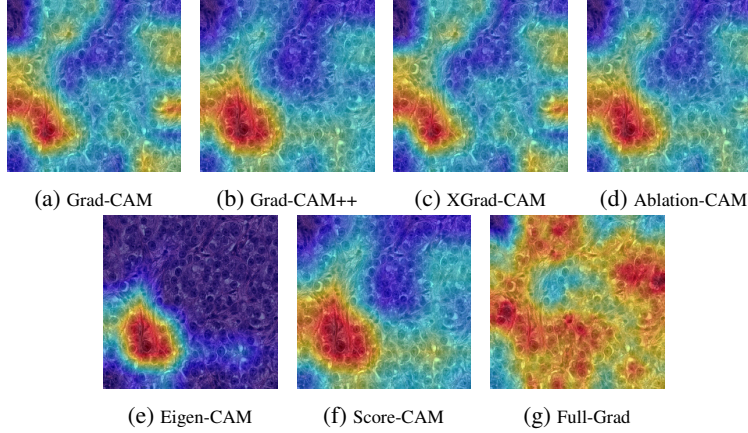


Figure 4: A sequence of images showcasing different CAM-based methods applied to the tumor patch for decision making. Each method provides a unique perspective on the activation areas within the image.

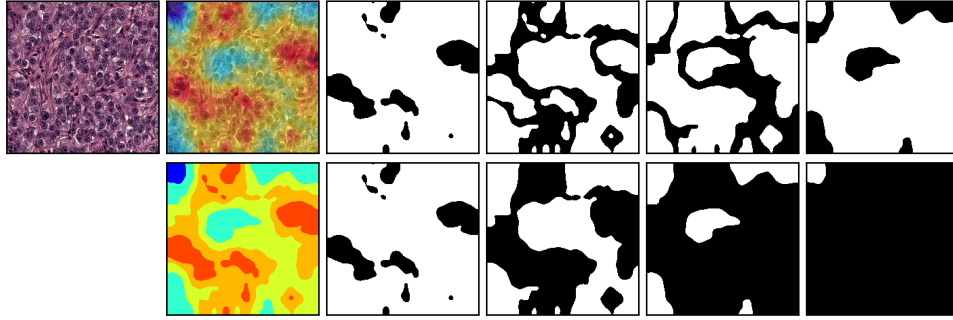


Figure 5: A sequence showing a tumor patch, its Full-Grad heatmap, and various masks. Line 1 displays the original tumor patch and its corresponding heatmap, with masks highlighting regions of varying importance from high to low. Line 2 illustrates that the black regions in each mask represent areas that have been occluded after each step. This sequence demonstrates the progressive occlusion of tumor regions based on their significance as indicated by the heatmap.

4.2 Evaluation of Inpainted Samples

The Learned Perceptual Image Patch Similarity (LPIPS) metric [47], is a widely recognized and effective measure for capturing perceptual differences between images. LPIPS is particularly well-suited for assessing image quality and dissimilarities, as it assigns higher values to pairs of images that are perceived as more dissimilar, thereby providing a robust evaluation of perceptual differences.

The LPIPS metric is defined as:

$$\text{LPIPS}(x, \hat{x}) = \sum_l \frac{1}{H_l W_l} \sum_{h=1}^{H_l} \sum_{w=1}^{W_l} \|\mathbf{w}_l \odot (\phi_l(x)_{hw} - \phi_l(\hat{x})_{hw})\|_2^2, \quad (7)$$

where x and \hat{x} are the original and reconstructed images, respectively, $\phi_l(\cdot)$ represents the deep features extracted from layer l of a pre-trained network, H_l and W_l are the height and width of the feature map at layer l , \mathbf{w}_l is a learned weight vector specific to layer l , and \odot denotes element-wise multiplication.

In our study, we utilize LPIPS with AlexNet [48] as the feature extraction network to quantify the perceptual differences between the original images and their corresponding occluded versions. Specifically, we compute LPIPS scores for image patches, comparing the original

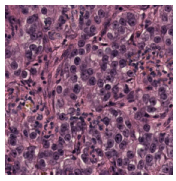
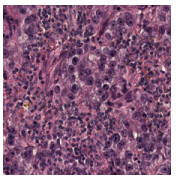
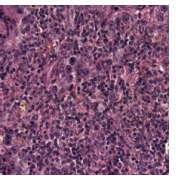
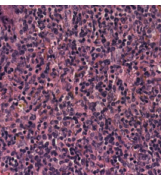
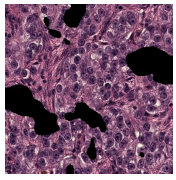
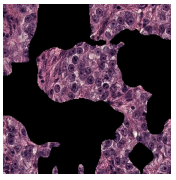
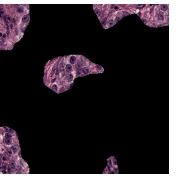

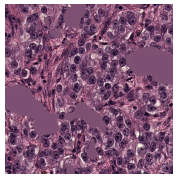
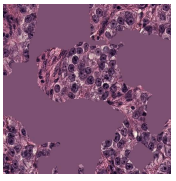
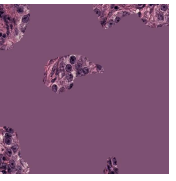

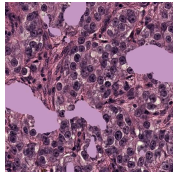
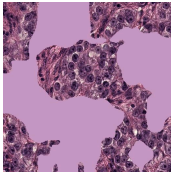


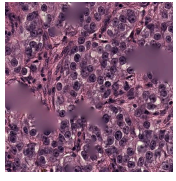
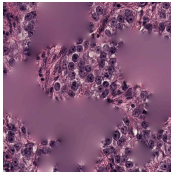
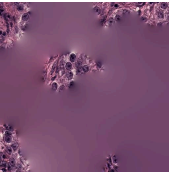

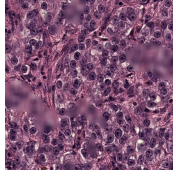
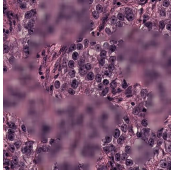
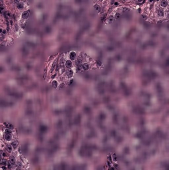
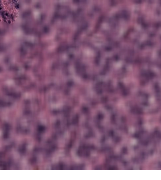
Occlusion Strategy	Mask ₁	Mask ₂	Mask ₃	Mask ₄
IBO				
Blackening				
Mean				
Histogram				
Noisy Linear Imputation				
Blurring				

Figure 6: Illustration of various occlusion strategies applied to masked patches.

patches with their reconstructions generated through various occlusion strategies. These LPIPS scores are then directly employed as an OoD detection metric. This methodology is based on the premise that perceptual metrics like LPIPS are particularly effective for inpainting tasks, as they are sensitive to subtle changes and anomalies, making them useful for identifying OoD samples. The detailed results of our LPIPS analysis are presented in Table 1.

Table 1: LPIPS Scores for different occlusion strategies. Each Mask_{*i*} corresponds to the inpainting of specific regions in the image, progressively targeting areas of decreasing importance as identified by the heatmap.

Occlusion Strategy	Mask ₁	Mask ₂	Mask ₃	Mask ₄
Blackening	0.1106	0.2280	0.3693	0.5567
Histogram	0.0841	0.1844	0.3082	0.4621
Mean	0.0796	0.1776	0.2997	0.4520
NLI	0.0781	0.1769	0.2999	0.4537
Blurring	0.0701	0.1593	0.2670	0.3895
IBO	0.0381	0.0826	0.1407	0.2180

4.3 Proposed framework quantitative evaluation

To evaluate our proposed occlusion approach, as shown in Table 2, we directly calculated the IoU between the ground-truth binary mask, indicating tumor regions in each sample, and the heatmap generated by the various XAI techniques. This process allowed us to create a ground-truth ranking for all XAI methods by averaging the IoU values across a test set of samples. The Intersection over Union IoU is defined as:

$$\text{IoU} = \frac{R_{\text{ht}} \cap R_{\text{gt}}}{R_{\text{ht}} \cup R_{\text{gt}}} \quad (8)$$

Where R_{ht} represents the region indicated by the heatmap, and R_{gt} denotes the ground truth region.

Table 2: IoU between ground-truth and heatmaps generated by CAM-based approaches. This ranking was used as ground-truth to evaluate occlusion strategies.

Approach	IoU
Full-Grad	0.6896
Grad-CAM	0.6482
Grad-CAM++	0.6467
XGrad-CAM	0.6464
Score-CAM	0.6452
Ablation-CAM	0.6439
Eigen-CAM	0.4257

To evaluate the effectiveness of heatmaps generated by CAM-based interpretability methods, we use the AUC to assess how well each heatmap correlates with the model’s tumor classification probability. Specifically, as we progressively occlude regions identified by the heatmaps as important, we track changes in the predicted probability of the tumor class. The AUC of this relationship measures the heatmap’s effectiveness.

In each occlusion step, we calculate the ratio of occluded regions to all identified regions, where a ratio of 0 means no regions are occluded and 1 indicates that all critical regions have been removed. A smaller AUC suggests that the occluded regions were crucial for tumor classification, implying that the heatmap effectively highlighted significant tumor-related areas. By comparing AUC values across different heatmap methods, we can identify which method most accurately captures critical regions relevant to the model’s decision-making.

For occlusion-based methods, including IBO, the AUC quantifies how the model’s tumor classification probability changes as progressively larger regions, identified as important by the heatmaps, are occluded. The AUC is defined as:

$$\text{AUC} = \int_0^1 f(p) dp \quad (9)$$

where $f(p)$ represents the tumor classification probability as a function of the percentage of occluded pixels, with p normalized to the range $[0, 1]$. Here, p ranges from 0 to 1, representing 0% to 100% occlusion, and $f(p)$ denotes the classification probability for the tumor given the percentage p of occluded pixels.

A lower AUC indicates that the occluded regions were critical to the model’s decision, signifying accurate heatmap highlighting. We compare AUC values from different heatmap methods to determine which technique best identifies key regions influencing the model’s tumor classification. Additionally, we compare the AUC rankings with those obtained using the IoU metric to find the most reliable occlusion method. The AUC values for various methods, including our IBO approach, are presented in Tables 3–8.

Table 3: IBO rankings

Approach	AUC
Full-Grad	0.5335
Grad-CAM	0.5991
Grad-CAM++	0.6014
XGrad-CAM	0.6058
Ablation-CAM	0.6363
Score-CAM	0.6707
Eigen-CAM	0.8622

Table 4: Blurring rankings

Approach	AUC
Full-Grad	0.4769
Grad-CAM	0.5360
XGrad-CAM	0.5360
Ablation-CAM	0.5651
Grad-CAM++	0.5898
Score-CAM	0.6094
Eigen-CAM	0.8511

Table 5: NLI rankings

Approach	AUC
Full-Grad	0.3788
Grad-CAM	0.4265
XGrad-CAM	0.4278
Ablation-CAM	0.4612
Grad-CAM++	0.4850
Score-CAM	0.5154
Eigen-CAM	0.7916

Table 6: Histogram rankings

Approach	AUC
Full-Grad	0.3823
Grad-CAM	0.4316
XGrad-CAM	0.4335
Ablation-CAM	0.4634
Grad-CAM++	0.4887
Score-CAM	0.5214
Eigen-CAM	0.7899

Table 7: Mean rankings

Approach	AUC
Full-Grad	0.3718
XGrad-CAM	0.4224
Grad-CAM	0.4233
Ablation-CAM	0.4537
Grad-CAM++	0.4790
Score-CAM	0.5078
Eigen-CAM	0.7871

Table 8: Blackening rankings

Approach	AUC
Full-Grad	0.4857
Grad-CAM++	0.5594
Grad-CAM	0.5624
Score-CAM	0.5897
Ablation-CAM	0.6061
XGrad-CAM	0.6290
Eigen-CAM	0.8630

Our approach demonstrates greater consistency in evaluating XAI methods compared to other occlusion-based strategies. Notably, five out of the seven XAI methods are ranked in the same order as in the IoU table, indicating that our method is superior for removing features depicted in heatmaps. This results in a 71% accuracy in predicting their performance outcomes, compared to 42% with the best-performing alternative, making our approach a more reliable tool for evaluating XAI methods. In addition, we evaluate the ranking performance of different methods by computing the Mean Absolute Rank Difference (MARD). MARD is a metric that quantifies the average deviation between the ranks assigned by a specific occlusion strategy and the ground-truth ranks. Mathematically, MARD is defined as follows:

$$\text{MARD} = \frac{1}{N} \sum_{i=1}^N |\text{Rank}_{\text{GT}}(i) - \text{Rank}_{\text{oc}}(i)| \quad (10)$$

where N is the total number of CAM-based approaches, $\text{Rank}_{\text{GT}}(i)$ denotes the ground-truth rank of CAM-based approach i , and $\text{Rank}_{\text{oc}}(i)$ represents the rank assigned by a particular occlusion strategy. To apply this metric, we first established a ground-truth ranking of methods based on predefined criteria. Subsequently, we compared this ground-truth ranking to the rankings generated by various occlusion strategies. The goal was to measure how closely each strategy’s ranking aligns with the ground-truth ranking. The results of this analysis are summarized in Table 9. The table presents the MARD values for each method, ranked from the highest to the lowest. A lower MARD value indicates a closer alignment with the ground-truth ranking, suggesting a better performance.

Table 9: MARD values for occlusion strategies.

Table	MARD Value
Mean	1.1428
Blackening	0.8571
Histogram	0.8571
NLI	0.8571
Blurring	0.8571
IBO	0.2857

5 Limitations and future work

While our proposed IBO strategy offers significant improvements in the evaluation of XAI methods by reducing the generation of OoD samples, it is not without limitations. One limitation of our IBO strategy is that, despite utilizing a DDPM, the inpainting process might not always maintain the full semantic integrity of the inpainted regions. The model, while effective in generating realistic non-cancerous tissue, may occasionally fail to capture the intricate details and variability of actual cancerous regions, which could affect the accuracy of the evaluation. Future work should focus on enhancing the DDPM or integrating advanced generative models that are better suited for preserving the complex features of histopathological images, thereby improving the fidelity of the inpainting process.

Another limitation lies in the computational intensity of the IBO strategy. The process of inpainting, particularly when applied iteratively across multiple masks, can be computationally expensive and time-consuming, which may not be practical for large-scale datasets or real-time applications. To address this, future research should explore optimizing the inpainting process for efficiency, potentially by developing more streamlined algorithms or leveraging hardware acceleration techniques such as GPU optimization, to make the approach more feasible for broader use.

Finally, our method primarily focuses on evaluating the impact of inpainting on tumor classification without fully exploring its effects on other potential applications within histopathological analysis, such as segmentation or multi-class classification. This narrow focus might limit the applicability of the method to broader tasks within medical imaging. Future work should aim to extend the IBO strategy to encompass a wider range of applications, investigating how inpainting can influence other key aspects of histopathological image analysis, and thus provide a more comprehensive evaluation framework for XAI methods.

6 Conclusion

In this paper, we proposed a novel IBO strategy aimed at improving the evaluation of XAI methods in histopathological image analysis. Our approach utilizes a DDPM to inpaint occluded regions with realistic, non-cancerous tissue, effectively reducing the generation of OoD samples that commonly arise in traditional occlusion strategies. This enhancement ensures that the evaluation of XAI methods remains accurate and reliable by maintaining the integrity of the original data distribution.

Our experiments on the CAMELYON16 dataset employed a two-phase evaluation approach. In the first phase, we used the LPIPS metric to measure the perceptual similarity between original and inpainted images, with lower LPIPS scores indicating lower OoD artifacts. Our IBO method achieved significantly lower LPIPS scores compared to other occlusion strategies, suggesting it better preserves the original tissue characteristics. In the second phase, we established a ground truth ranking of XAI methods using IoU scores and then evaluated these methods with the IBO strategy and other approaches. By calculating the MARD, we found that the IBO method provided rankings much closer to the ground truth, demonstrating its superior accuracy in comparing XAI methods.

In conclusion, the IBO strategy not only enhances the interpretability of deep learning models in histopathology but also sets a new standard for the evaluation of XAI methods by

improving the accuracy of effectiveness rankings. The ability of IBO to generate more realistic inpainted regions and provide more reliable XAI evaluations underscores its potential for broader application in medical imaging.

List of Acronyms

XAI	Explainable Artificial Intelligence
AI	Artificial Intelligence
NLI	Noisy Linear Imputation
CNN	Convolutional Neural Network
OoD	Out-of-Distribution
WSI	whole slide image
AUC	Area Under the Curve
CAM	Class Activation Mapping
DDPM	Denoising Diffusion Probabilistic Model
IoU	Intersection over Union
IBO	Inpainting-Based Occlusion
LPIPS	Learned Perceptual Image Patch Similarity
MARD	Mean Absolute Rank Difference
XML	Extensible Markup Language
WCSS	Within-Cluster Sum of Squares

References

- [1] Neslihan Bayramoglu, Juho Kannala, and Janne Heikkilä. Deep learning for magnification independent breast cancer histopathology image classification. In *2016 23rd International Conference on Pattern Recognition (ICPR)*, pages 2440–2445, 2016. doi:10.1109/ICPR.2016.7900002.
- [2] Neofytos Dimitriou, Ognjen Arandjelović, and Peter D Caie. Deep learning for whole slide image analysis: an overview. *Frontiers in medicine*, 6:264, 2019.
- [3] Robert Beyer, Ali Rabiee, Sarah Ostadabbas, and Reza Abiri. Human-inspired vision-based reaching and grasping for assistive robotic arms with reinforcement learning. In *society for neuroscience*, 2023.
- [4] Kausik Das, Sailesh Conjeti, Jyotirmoy Chatterjee, and Debdoot Sheet. Detection of breast cancer from whole slide histopathological images using deep multiple instance cnn. *IEEE Access*, 8:213502–213511, 2020. doi:10.1109/ACCESS.2020.3040106.
- [5] Adriano Lucieri, Muhammad Naseer Bajwa, Andreas Dengel, and Sheraz Ahmed. Achievements and challenges in explaining deep learning based computer-aided diagnosis systems. *arXiv preprint arXiv:2011.13169*, 2020.
- [6] Mohammed M. Abdelsamea, Usama Zidan, Zakaria Senousy, Mohamed Medhat Gaber, Emad Rakha, and Mohammad Ilyas. A survey on artificial intelligence in histopathology image analysis. *WIREs Data Mining and Knowledge Discovery*, 12(6):e1474, 2022. doi:https://doi.org/10.1002/widm.1474. URL https://wires.onlinelibrary.wiley.com/doi/abs/10.1002/widm.1474.
- [7] Pouya Khani, Elham Moeinaddini, Narges Dehghan Abnavi, and Amin Shahraki. Explainable artificial intelligence for feature selection in network traffic classification: A comparative study. *Transactions on Emerging Telecommunications Technologies*, 35(4):e4970, 2024.
- [8] Amirhossein Aminimehr, Pouya Khani, Amirali Molaei, Amirmohammad Kazemeini, and Erik Cambria. Tbxplain: A text-based explanation method for scene classification models with the statistical prediction correction. In *Proceedings of the Conference on Governance, Understanding and Integration of Data for Effective and Responsible AI*, pages 54–60, 2024.
- [9] Ali Rabiee, Sima Ghafoori, Anna Cetera, and Reza Abiri. Wavelet analysis of non-invasive eeg signals discriminates complex and natural grasp types. *arXiv preprint arXiv:2402.09447*, 2024.
- [10] Akif Burak Tosun, Filippo Pullara, Michael J. Becich, D. Lansing Taylor, S. Chakra Chennubhotla, and Jeffrey L. Fine. *HistoMapr™: An Explainable AI (xAI) Platform for Computational Pathology Solutions*, pages 204–227. Springer International Publishing, Cham, 2020. ISBN 978-3-030-50402-1. doi:10.1007/978-3-030-50402-1_13. URL https://doi.org/10.1007/978-3-030-50402-1_13.
- [11] Bas H.M. van der Velden, Hugo J. Kuijf, Kenneth G.A. Gilhuijs, and Max A. Viergever. Explainable artificial intelligence (xai) in deep learning-based medical image analysis. *Medical Image Analysis*, 79:102470, 2022. ISSN 1361-8415. doi:https://doi.org/10.1016/j.media.2022.102470. URL https://www.sciencedirect.com/science/article/pii/S1361841522001177.
- [12] Yi-Shan Lin, Wen-Chuan Lee, and Z Berkay Celik. What do you see? evaluation of explainable artificial intelligence (xai) interpretability through neural backdoors. In *Proceedings of the 27th ACM SIGKDD conference on knowledge discovery & data mining*, pages 1027–1035, 2021.
- [13] Zana Buçinca, Phoebe Lin, Krzysztof Z. Gajos, and Elena L. Glassman. Proxy tasks and subjective measures can be misleading in evaluating explainable ai systems. In *Proceedings of the 25th International Conference on Intelligent User Interfaces*, IUI

- '20. ACM, March 2020. doi:10.1145/3377325.3377498. URL <http://dx.doi.org/10.1145/3377325.3377498>.
- [14] Richard Tomsett, Dan Harborne, Supriyo Chakraborty, Prudhvi Gurram, and Alun Preece. Sanity checks for saliency metrics. In *Proceedings of the AAAI conference on artificial intelligence*, volume 34, pages 6021–6029, 2020.
- [15] Chih-Kuan Yeh, Cheng-Yu Hsieh, Arun Sai Suggala, David I. Inouye, and Pradeep Ravikumar. On the (in)fidelity and sensitivity for explanations, 2019. URL <https://arxiv.org/abs/1901.09392>.
- [16] Matthew D Zeiler and Rob Fergus. Visualizing and understanding convolutional networks. *arXiv preprint arXiv:1311.2901*, 2014.
- [17] Maksims Ivanovs, Roberts Kadikis, and Kaspars Ozols. Perturbation-based methods for explaining deep neural networks: A survey. *Pattern Recognition Letters*, 150:228–234, 2021. ISSN 0167-8655. doi:<https://doi.org/10.1016/j.patrec.2021.06.030>. URL <https://www.sciencedirect.com/science/article/pii/S0167865521002440>.
- [18] Wojciech Samek, Alexander Binder, Grégoire Montavon, Sebastian Lapuschkin, and Klaus-Robert Müller. Evaluating the visualization of what a deep neural network has learned. *IEEE transactions on neural networks and learning systems*, 28(11):2660–2673, 2016.
- [19] Miquel Miró-Nicolau, Antoni Jaume i Capó, and Gabriel Moyà-Alcover. A comprehensive study on fidelity metrics for xai, 2024. URL <https://arxiv.org/abs/2401.10640>.
- [20] Tristan Gomez, Thomas Fréour, and Harold Mouchère. Metrics for saliency map evaluation of deep learning explanation methods, 2022. URL <https://arxiv.org/abs/2201.13291>.
- [21] Pieter-Jan Kindermans et al. The (un)reliability of saliency methods. In *Explainable AI: Interpreting, Explaining and Visualizing Deep Learning*, pages 267–280. Springer, 2019.
- [22] Sanjoy Dasgupta, Nathan Frost, and Martin Moshkovitz. Framework for evaluating faithfulness of local explanations. In *Proceedings of the 39th International Conference on Machine Learning*, pages 4794–4815. PMLR, 2022.
- [23] Meike Nauta et al. From anecdotal evidence to quantitative evaluation methods: a systematic review on evaluating explainable ai. *ACM Computing Surveys (CSUR)*, 55(13s):1–42, 2023.
- [24] Vangelis Lamprou, Athanasios Kallipolitis, and Ilias Maglogiannis. On the evaluation of deep learning interpretability methods for medical images under the scope of faithfulness. *Computer Methods and Programs in Biomedicine*, page 108238, 2024.
- [25] S Rajaraman, S Candemir, G Thoma, and S Antani. Visualizing and explaining deep learning predictions for pneumonia detection in pediatric chest radiographs. In *Medical Imaging: Computer-Aided Diagnosis*, volume 10950. SPIE, 2019.
- [26] Rory Sayres et al. Using a deep learning algorithm and integrated gradients explanation to assist grading for diabetic retinopathy. *Ophthalmology*, 126(4):552–564, 2019.
- [27] Mukund Sundararajan, Ankur Taly, and Qiqi Yan. Axiomatic attribution for deep networks, 2017. URL <https://arxiv.org/abs/1703.01365>.
- [28] Mara Graziani, Thomas Lompech, Henning Müller, and Vincent Andrearczyk. Evaluation and comparison of cnn visual explanations for histopathology. In *Proceedings of the AAAI Conference on Artificial Intelligence Workshops (XAI-AAA-21), Virtual Event*, pages 8–9, 2021.

- [29] Richard Tomsett, Dan Harborne, Supriyo Chakraborty, Prudhvi Gurram, and Alun Preece. Sanity checks for saliency metrics, 2019. URL <https://arxiv.org/abs/1912.01451>.
- [30] Ruth C. Fong and Andrea Vedaldi. Interpretable explanations of black boxes by meaningful perturbation. In *2017 IEEE International Conference on Computer Vision (ICCV)*. IEEE, October 2017. doi:10.1109/iccv.2017.371. URL <http://dx.doi.org/10.1109/ICCV.2017.371>.
- [31] Yi Wei, Ming-Ching Chang, Yiming Ying, Ser Nam Lim, and Siwei Lyu. Explain black-box image classifications using superpixel-based interpretation. In *2018 24th International Conference on Pattern Recognition (ICPR)*, pages 1640–1645, 2018. doi:10.1109/ICPR.2018.8546302.
- [32] Yao Rong, Tobias Leemann, Vadim Borisov, Gjergji Kasneci, and Enkelejda Kasneci. A consistent and efficient evaluation strategy for attribution methods. *arXiv preprint arXiv:2202.00449*, 2022.
- [33] Jonathan Ho, Ajay Jain, and Pieter Abbeel. Denoising diffusion probabilistic models, 2020. URL <https://arxiv.org/abs/2006.11239>.
- [34] Andreas Lugmayr, Martin Danelljan, Andres Romero, Fisher Yu, Radu Timofte, and Luc Van Gool. Repaint: Inpainting using denoising diffusion probabilistic models, 2022. URL <https://arxiv.org/abs/2201.09865>.
- [35] Maxime Oquab, Leon Bottou, Ivan Laptev, and Josef Sivic. Is object localization for free? - weakly-supervised learning with convolutional neural networks. In *Proceedings of the IEEE Conference on Computer Vision and Pattern Recognition (CVPR)*, June 2015.
- [36] J. A. Hartigan and M. A. Wong. A k-means clustering algorithm. *JSTOR: Applied Statistics*, 28(1):100–108, 1979.
- [37] Diagnostic Assessment of Deep Learning Algorithms for Detection of Lymph Node Metastases in Women With Breast Cancer. *JAMA*, 318(22):2199–2210, 2017.
- [38] Santanu Roy, Shubhajit Panda, and Mahesh Jangid. Modified reinhard algorithm for color normalization of colorectal cancer histopathology images. In *2021 29th European Signal Processing Conference (EUSIPCO)*, pages 1231–1235, 2021. doi:10.23919/EUSIPCO54536.2021.9616117.
- [39] Kaiming He, Xiangyu Zhang, Shaoqing Ren, and Jian Sun. Deep residual learning for image recognition, 2015. URL <https://arxiv.org/abs/1512.03385>.
- [40] Ramprasaath R. Selvaraju, Michael Cogswell, Abhishek Das, Ramakrishna Vedantam, Devi Parikh, and Dhruv Batra. Grad-cam: Visual explanations from deep networks via gradient-based localization. *International Journal of Computer Vision*, 128(2): 336–359, October 2019. ISSN 1573-1405. doi:10.1007/s11263-019-01228-7. URL <http://dx.doi.org/10.1007/s11263-019-01228-7>.
- [41] Aditya Chattopadhyay, Anirban Sarkar, Prantik Howlader, and Vineeth N Balasubramanian. Grad-cam++: Generalized gradient-based visual explanations for deep convolutional networks. In *2018 IEEE Winter Conference on Applications of Computer Vision (WACV)*, pages 839–847, 2018. doi:10.1109/WACV.2018.00097.
- [42] Ruigang Fu, Qingyong Hu, Xiaohu Dong, Yulan Guo, Yinghui Gao, and Biao Li. Axiom-based grad-cam: Towards accurate visualization and explanation of cnns, 2020. URL <https://arxiv.org/abs/2008.02312>.
- [43] Saurabh Desai and Harish G. Ramaswamy. Ablation-cam: Visual explanations for deep convolutional network via gradient-free localization. In *2020 IEEE Winter Conference on Applications of Computer Vision (WACV)*, pages 972–980, 2020. doi:10.1109/WACV45572.2020.9093360.

- [44] Mohammed Bany Muhammad and Mohammed Yeasin. Eigen-cam: Class activation map using principal components. In *2020 International Joint Conference on Neural Networks (IJCNN)*. IEEE, July 2020. doi:10.1109/ijcnn48605.2020.9206626. URL <http://dx.doi.org/10.1109/IJCNN48605.2020.9206626>.
- [45] Haofan Wang, Zifan Wang, Mengnan Du, Fan Yang, Zijian Zhang, Sirui Ding, Piotr Mardziel, and Xia Hu. Score-cam: Score-weighted visual explanations for convolutional neural networks, 2020. URL <https://arxiv.org/abs/1910.01279>.
- [46] Suraj Srinivas and Francois Fleuret. Full-gradient representation for neural network visualization, 2019. URL <https://arxiv.org/abs/1905.00780>.
- [47] Richard Zhang, Phillip Isola, Alexei A. Efros, Eli Shechtman, and Oliver Wang. The unreasonable effectiveness of deep features as a perceptual metric, 2018. URL <https://arxiv.org/abs/1801.03924>.
- [48] Alex Krizhevsky, Ilya Sutskever, and Geoffrey E. Hinton. Imagenet classification with deep convolutional neural networks. In *Proceedings of the 25th International Conference on Neural Information Processing Systems - Volume 1, NIPS'12*, page 1097–1105, Red Hook, NY, USA, 2012. Curran Associates Inc.